



1 **Understanding summertime peroxyacetyl nitrate (PAN) formation and**
2 **its relation to aerosol pollution: Insights from high-resolution**
3 **measurements and modeling**

4 **Baoye Hu^{1,3,4}, Naihua Chen^{1,6}, Rui Li⁷, Mingqiang Huang^{1,3,4}, Jinsheng Chen^{2,5*}, Youwei Hong^{2,5},**
5 **Lingling Xu^{2,5}, Xiaolong Fan^{2,5}, Mengren Li^{2,5}, Lei Tong², Qiuping Zheng⁸, Yuxiang Yang^{6*}**

6 ¹College of Chemistry, Chemical Engineering and Environment, Minnan Normal University, Zhangzhou, China, 363000

7 ²Center for Excellence in Regional Atmospheric Environment, Institute of Urban Environment, Chinese Academy of Sciences,
8 Xiamen 361021, China

9 ³Fujian Provincial Key Laboratory of Modern Analytical Science and Separation Technology, Minnan Normal University,
10 Zhangzhou, China, 363000

11 ⁴Fujian Province University Key Laboratory of Pollution Monitoring and Control, Minnan Normal University, Zhangzhou, China,
12 363000

13 ⁵Fujian Key Laboratory of Atmospheric Ozone Pollution Prevention, Chinese Academy of Sciences, Xiamen 361021, China

14 ⁶Pingtang Environmental Monitoring Center of Fujian, Pingtan 350400, China

15 ⁷Key Laboratory of Geographic Information Science of the Ministry of Education, School of Geographic Science, East China
16 Normal University, Shanghai 200241, PR China

17 ⁸Xiamen Key Laboratory of Straits Meteorology, Xiamen Meteorological Bureau, Xiamen 361012, China

18 *Correspondence to:* Jinsheng Chen (jschen@iue.ac.cn) & Yuxiang Yang (907460293@qq.com)

19

20 **Abstract:** Peroxyacetyl nitrate (PAN), a key indicator of photochemical pollution, is generated through a process similar to ozone
21 (O_3), involving the photochemical reactions of specific volatile organic compounds (VOCs) in the presence of nitrogen oxides.
22 Notably, PAN has been observed at unexpectedly high concentrations (maximum: 3.04 ppb) during summertime that the daily
23 maximum values of PAN were better correlated to black carbon (BC) ($R^2=0.85$) than ozone (O_3) ($R^2=0.75$), suggesting that
24 summertime haze and photochemical pollution were deeply connected. We addressed the puzzle of summertime PAN formation
25 and its association with aerosol pollution under high ozone conditions by analyzing continuous high temporal resolution data
26 utilizing box modeling in conjunction with the master chemical mechanism (MCM). With an IOA value of 0.75, the MCM model
27 proves to be an ideal tool for investigating PAN photochemical formation. The model performed better during the clean period (R^2 :
28 0.6782, slope K: 0.9097) than during the haze period (R^2 : 0.4708, slope K: 0.7477). Through the machine learning method of
29 XGBoost, we found that the top three factors leading to simulation bias were NH_3 , NO_3 , and $PM_{2.5}$. Moreover, the net production



30 rate of PAN becomes negative with PAN constrained, suggesting the existence of an unknown compensatory mechanism. Both
31 RIR and EKMA analyses indicate that PAN formation in this region is VOC-controlled. Controlling emissions of VOCs,
32 particularly alkenes, C₅H₈, and aromatics, would mitigate PAN pollution. RIR results also show that during the clean period, PAN
33 is more sensitive to changes in various pollutants than during the haze period, underscoring the importance of deep emission
34 reductions. PAN promotes OH and HO₂ while inhibiting the formation of O₃, RO₂, NO, and NO₂. This study deepens our
35 comprehension of PAN photochemistry while also offering scientific insights for guiding future PAN pollution control strategies.

36

37 **Introduction**

38 Peroxyacetyl nitrate (PAN, CH₃C(O)ONO₂) is a significant secondary gaseous pollutant commonly present in photochemical
39 smog and poses risk to human health and plant growth, being 1-2 magnitudes more phytotoxic than ozone (O₃) (Yukihiro et al.,
40 2012; Taylor, 1969). Additionally, PAN's low aqueous solubility, minimal reactivity with hydroxyl radicals (OH), and slow
41 photolysis contribute to its capacity for long-range transport of nitrogen oxides (NO_x) (Xu et al., 2018; Zhai et al., 2024; Marley
42 et al., 2007b). Therefore, its formation in polluted areas holds significant importance beyond local concerns. Similar to surface O₃,
43 PAN is produced during the oxidation of volatile organic compounds (VOCs) in the presence of NO_x (R1-R3). PAN is formed
44 when NO₂ reacts with peroxyacetyl (PA) radicals (CH₃C(O)OO•) (R2), but the presence of NO consumes PA radicals, inhibiting
45 PAN production (R3), which creates a comparable dependence of PAN and O₃ on NO and NO₂ levels (Xu et al., 2021). Unlike O₃,
46 however, PAN is influenced by only a limited number of oxygenated VOCs (OVOCs) that generate PA radicals. These OVOCs,
47 which are second-generation precursors of PAN, include acetaldehyde (CH₃CHO), acetone (CH₃C(O)CH₃), methylglyoxal
48 (MGLY, CH₃C(O)CHO), methyl vinyl ketone (MVK, CH₂CHC(O)CH₃), methyl ethyl ketone (MEK, CH₃C(O)CH₂CH₃),
49 methacrolein (MACR, CH₂C(CH₃)CHO), and biacetyl (CH₃C(O)C(O)CH₃). These compounds are typically formed from the
50 oxidation of alkenes, aromatics, and isoprene, which are the first-generation precursors of PAN (Xue et al., 2014; Zhang et al.,
51 2015). Identifying the dominant precursors is crucial for managing PAN pollution effectively. In the troposphere, thermal
52 decomposition (R4) is the primary process responsible for PAN loss (Xu et al., 2021).



57 In recent years, wintertime photochemical air pollution has increasingly garnered attention. At this time, the concentration of O₃ is
58 low due to the strong titration of NO, while the concentration of aerosol is high, and it is found that aerosol promotes PAN
59 generation. Surprisingly high concentrations of OH radical, particularly under hazy conditions, have been observed and are largely



60 attributed to HONO photolysis. Winter photochemical and haze pollution often exacerbate each other, with photochemical trace
61 gases supplying both oxidants and precursors for aerosol formation, and aerosols acting as mediums for heterogeneous reactions
62 that produce key oxidants such as HONO, H₂O₂, and OH radicals (Xu et al., 2021). The OH produced by HONO photolysis can
63 partially replace the UV action to promote PAN formation in winter in southeast coastal area of China when particulate matter is
64 high ($\geq 35\mu\text{g}\cdot\text{m}^{-3}$) (Hu et al., 2020). Zhang et al. (2020) found the potential HONO sources significantly improved the PAN
65 simulations in wintertime heavy haze events with high concentrations of PAN. High concentrations of PAN are a consequence of
66 the increased levels of precursors and HONO observed during haze episodes (Liu et al., 2018). In conclusion, most previous
67 studies have studied the effect of aerosol on PAN generation in winter. Further research on PAN should determine whether
68 particulates significantly contribute to its formation during warmer seasons with elevated ozone concentrations (Xu et al., 2021).
69 In Eastern China, photochemical air pollution often involves high concentrations of both O₃ and PAN, a persistent issue during the
70 warm season (April-September) for many years (Lu et al., 2020). The characteristics and formation pathways of PAN during
71 summer have been increasingly studied in regions such as the North China Plain (NCP), the Yangtze River Delta, the Pearl River
72 Delta, and southwestern China. These studies have generally shown consistent diurnal patterns and strong correlations between
73 PAN and O₃, identifying acetaldehyde—primarily derived from the degradation of aromatics and alkenes—as the key direct
74 precursor of PAN in the summer. However, there has been limited research on the formation of peroxyacetyl nitrate (PAN) and its
75 relationship with aerosol pollution during the summertime.

76 Ximen is one of the fastest urbanizing regions in the southeast China and is also one of the cities with the best air quality in China,
77 where the air quality could represent the future of other Chinese urban regions. Xiamen is also often affected by typhoons and
78 subtropical weather forms in summer. The West Pacific Subtropical High (WPSH) creates weather conditions that promote the
79 formation and accumulation of photochemical pollutants and particulate matter (Wu et al., 2019). This setting provides an ideal
80 "laboratory" for investigating the complexities of summertime PAN formation and its relationship with aerosol pollution under
81 high ozone concentrations. In this study, continuous measurements of trace gases, substances related to aerosols, photolysis rate
82 constants and meteorological parameters were performed at a suburban site in Xiamen from July 10th to July 31st, 2018. Firstly,
83 we provide an overview of pollutant concentrations, meteorological parameters, and weather conditions during the observation
84 period. Secondly, we simulate PAN concentration with the aid of box modeling combined with master chemical mechanism
85 (MCM). Using a machine learning-XGBoost looks for the key factors that affect the model's simulation result and clarified the
86 mechanisms linking haze pollution to photochemical air pollution, as indicated by PAN and O₃. Thirdly, the study identified the
87 main precursors and oxidants responsible for summertime PAN production in Xiamen and evaluated the influence of PAN on local
88 atmospheric oxidation capacity. This study further emphasized the interplay between haze and photochemical air pollution and
89 highlighted significant implications for future research.

90



91 **2 Methodology**

92 **2.1 Field observations**

93 Trace gases (including PAN, O₃, HONO, HNO₃, HCl, NH₃, VOCs, NO_x, CO, and SO₂), substances related to aerosols (including
94 BC, PM₁, PM_{2.5}, PM₁₀, SO₄²⁻, NO₃⁻, NH₄⁺, Cl⁻, Na⁺, K⁺, Ca²⁺, Mg²⁺), photolysis rate constants (including JO¹D, JNO₂, JHONO,
95 JHCHO_M, JHCHO_R, JNO₃_M, JNO₃_R, JH₂O₂), and meteorological parameters (including temperature, relative humidity,
96 atmospheric pressure, wind speed, and wind direction) were continuously measured at an suburban site in Xiamen from July 10th
97 to July 31st, 2018. All instruments were placed inside an air-conditioned container situated on the rooftop of a 20-story building at
98 the Institute of Urban Environment, Chinese Academy of Sciences (IUE: 118.06°E, 24.61°N) (Fig. S1(a)). When southerly winds
99 prevailed, Xiamen Island, characterized by dense population and traffic congestion, was located upwind of the IUE (Fig. S1(b)).
100 The IUE supersite is surrounded by Xinglin Bay, several universities and institutes, and major roadways with heavy traffic, such
101 as Jimei Road (< 200 m), Shenhai Expressway (870 m), and Xiasha Expressway (2300 m) (Fig. S1(c)).
102 PAN measurements were conducted using a PANs-1000 analyzer (Focused Photonics Inc., Hangzhou, China), which features an
103 automated system consists of a gas chromatograph, an electron capture detector, and a calibration unit. The analyzer provided
104 PAN readings every 5 minutes, with a detection limit of 50 ppt. The uncertainty and precision of the PAN measurements were ±10%
105 and 3%, respectively. The PAN standard gas was produced through the reaction of acetone and NO under UV light. Calibration
106 procedures included monthly multi-point calibrations and weekly single-point calibrations. Detailed information about the PAN
107 detection system and calibration can be found in previous studies (Hu et al., 2020; Liu et al., 2022). HONO measurements were
108 conducted using a customized Incoherent BroadBand Cavity Enhanced Absorption Spectroscopy (IBBCEAS) system developed
109 by the Anhui Institute of Optics and Fine Mechanics (AIOFM), Chinese Academy of Sciences. The HONO detection limit was
110 100 ppt, with a time resolution of 1 minute. The measurement principle and calibration method of IBBCEAS can be found in the
111 previous literature (Hu et al., 2022; Duan et al., 2018; Hu et al., 2024). The concentrations of inorganic components in PM_{2.5}
112 aerosols (including SO₄²⁻, NO₃⁻, NH₄⁺, Cl⁻, Na⁺, K⁺, Ca²⁺, Mg²⁺), as well as the concentrations of gases such as NH₃, HCl, and
113 HNO₃ were analyzed using a Monitor for AeRosols and Gases in ambient Air (MARGA, Model ADI 2080, Applikon Analytical
114 B.V., the Netherlands) (Hu et al., 2022). The criteria air pollutants O₃, NO_x, CO, and SO₂ were measured using different methods:
115 ultraviolet (UV) absorption for O₃ (TEI model 49i), chemiluminescence with a molybdenum converter for NO_x (TEI model 42i),
116 non-dispersive infrared for CO (TEI model 48i), and pulsed UV fluorescence for SO₂ (TEI model 43i). A tapered element
117 oscillating microbalance (TEOM1405, Thermo Scientific Corp., MA, USA) was used to continuously measure the mass
118 concentrations of PM₁, PM_{2.5}, and PM₁₀ online. A photolysis spectrometer (PFS-100, Focused Photonics Inc., Hangzhou, China)
119 was employed to measure the photolysis rate constants. An ultrasonic atmosphere (150WX, Airmar, USA) was used to measure
120 meteorological parameters.

121



122 **2.2 Box modeling**

123 This study employed a box model framework utilizing the Master Chemical Mechanism (MCMv3.3.1,
124 <https://mcm.york.ac.uk/MCM/home.htm>) to investigate sensitivity and mechanisms of PAN formation. The model constraints were
125 derived from observations of trace gases and meteorological parameters, which were averaged to 1-hour intervals. The reliability
126 of model simulation results is often assessed using the index of agreement (IOA), which ranges from 0 to 1, with a higher IOA
127 signifying greater alignment between observed and simulated values. Note that the model simulation values at this time are not
128 constrained by PAN. For specific formulas, please refer to the supplementary information (Eq. S1). Other formulas, including
129 PAN production rates ($P(\text{PAN})$), net production of PAN (Net (PAN)), and the relative incremental reactivity (RIR), are provided in
130 the supplementary information (Eq. S2- Eq. S4).

131 The MCM simulates the nonlinear interaction between PAN and its precursors by altering the VOCs-to-NO_x ratio across multiple
132 scenarios, while keeping all other parameters fixed. In this study, a 20% step size was applied, reducing VOCs and NO_x from 200%
133 down to 0% to construct a scenario matrix. A total of 121 scenarios were generated to model the PAN production rate. The
134 scenario representing the average VOCs and NO_x mixing ratio during the sampling period was designated as the base case, with
135 the remaining 120 scenarios created by systematically adjusting the VOC-to-NO_x ratio. The output from these 121 simulations
136 was used to construct isopleth diagrams depicting the relationship between VOCs, NO_x, and PAN.

137 **2.3 Machine Learning Model**

138 To identify the key factors influencing the performance of the model simulation, the Machine Learning (ML) model was applied
139 to establish the prediction model of bias between simulation of OBM and observation. XGBoost is a supervised boosting
140 algorithm that reduces the risk of over-fitting, captures the nonlinear relationships among predictor variables, and solves numerous
141 data science problems in a rapid and accurate way (Li et al., 2024). It has demonstrated high performance in O₃ studies in over
142 China. As compared to other bagging tree models like random forest, XGBoost can handle more complex data while consuming
143 fewer computing resources. To further improve the interpretability of the ML model, the feature importance of independent input
144 variables in the XGBoost model is quantified using the Shaply Additive explanation (SHAP) approach. The SHAP calculates a
145 value that represents the contribution of each feature to the model's outcome, which has been successfully applied in atmospheric
146 environmental studies. When the model was being adjusted, 90% of the data was used as the training set, and 10% of the data was
147 used as the test set. The hyperparameters were tuned using grid search and cross-validation method. Specifically, for a single
148 hyperparameter, grid search was used to obtain its more appropriate value range, and for the combinations of hyperparameters, the
149 whole training set was split into ten folds and then run a grid search over pre-adjusted combinations of hyperparameters by
150 training nine folds and predicting on the one fold in cross-validation procedure. For key hyperparameters of XGBoost model, the
151 number of trees was 100, learning rate was 0.1, max depth was 6. The model was trained and tested on hourly data during the
152 whole observation and the established model was examined by coefficient of determination (R^2) value, the root-mean-squared



153 error (RMSE) and mean absolute error (MAE). The formulas of RMSE and MAE are provided in the supplementary information
154 (Eq. S5 & Eq. S6). The performance of both models is illustrated in Fig. S3. The R^2 , MAE, and RMSE for the training set are
155 0.9037, 0.08, and 0.12, respectively, while the corresponding values for the test set are 0.7664, 0.10, and 0.14, respectively. These
156 statistical metrics indicate that the XGBoost model is promising for further analysis.

157

158 **3. Results and discussion**

159 **3.1 Overview of observation**

160 The measured data of PAN, related trace gases and meteorological parameters at IUE over 10-31 July 2018 are documented in Fig.

161 1. Combine with the synoptic situation (Fig. S4), the 8th typhoon of 2018, Typhoon Maria, made landfall on the morning of the
162 11th in Huangqi Peninsula, Lianjiang County, Fujian. Due to the influence of the typhoon's outer spiral rain bands, there was
163 moderate to heavy rain on the 11th. Correspondingly, there was a noticeable decrease in ultraviolet radiation and the temperatures.

164 Starting from the 12th, a Western Pacific subtropical high (WPSH) strengthened and extended westward, exerting control over
165 Xiamen city. In the lower atmosphere, it was influenced by the eastward flow, resulting in predominantly cloudy weather. From
166 the 16th to the 18th, the area was affected by the outer periphery of Typhoon Shan Shen, which formed on the 17th in the
167 northeastern part of the South China Sea and moved westward, making landfall along the coast of Wancheng Town, Wanning City,
168 Hainan Province in the early hours of the 18th. During this period, the city experienced strong winds with gusts reaching 5 to 6 on

169 the Beaufort scale in the urban areas. At the same time, the concentration of various pollutants reached their lowest levels, and the
170 daily variation patterns were less pronounced. From the 20th to the 21st, Xiamen City experienced the influence of the peripheral
171 descending airflow associated with Typhoon Ampil (which formed in the northwest Pacific Ocean around 8:00 P.M. on the 18th

172 and moved northwest, making landfall along the coast of Chongming Island, Shanghai, around noon on the 22nd). During this
173 period, there were fewer clouds and higher temperatures. From the 22nd to the 24th, the city was successively affected by the
174 outer periphery of Typhoon Ampil and a tropical low-pressure system, resulting in occasional showers or thunderstorms. From the

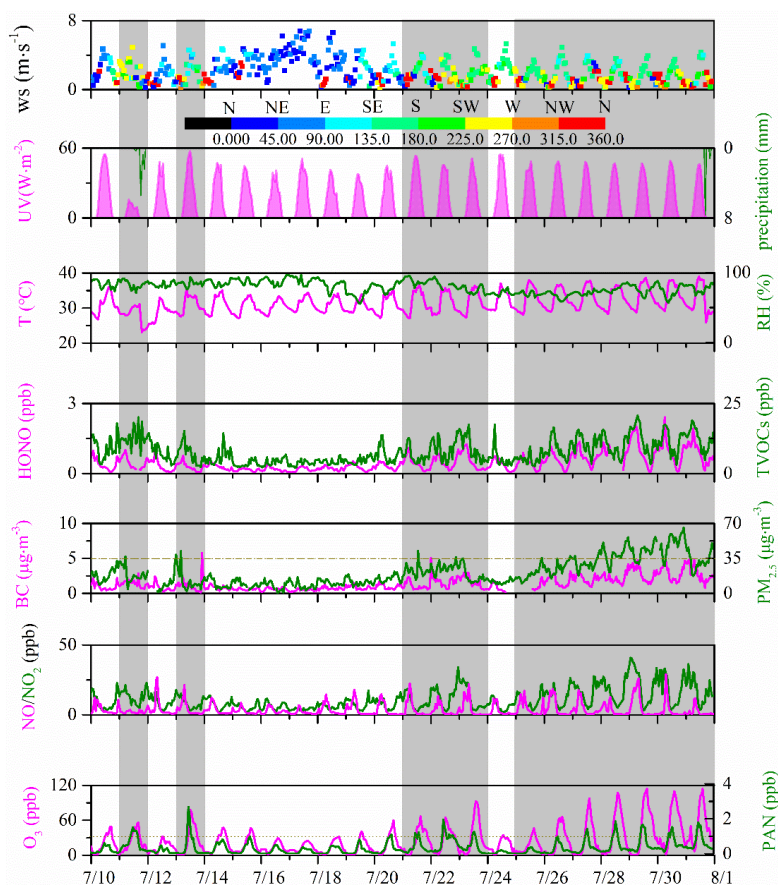
175 25th to the 31st, a WPSH once again strengthened and controlled Xiamen City. As a result, Xiamen city experienced stable
176 meteorological conditions, with light winds ($w_s = 1.04$ m/s), persistently high temperatures (daily maximum average of 37.82°C),
177 and high relative humidity (daily maximum average of 81.65%). These factors created an environment that favored the buildup of

178 particulate matter and enhanced the photochemical formation of O_3 and PAN (Wu et al., 2019). The daily maximum average of
179 $\text{PM}_{2.5}$, O_3 and PAN were $49.26 \mu\text{g}\cdot\text{m}^{-3}$, 93.62 ppb, and 1.37 ppb, respectively.

180 The phenomenon of simultaneous high levels of photochemical and particulate matter appears. Throughout the 22-days campaign,
181 12 days (including July 11th, 13th, 21st to 23rd, and 25th to 31st) were observed with 1 h concentrations of $\text{PM}_{2.5}$ exceeding 35
182 $\mu\text{g}\cdot\text{m}^{-3}$; 13 days (including July 11th, 13th, 15th, 20th to 23rd, and 26th to 31st) were observed with 5-min concentrations of PAN
183 exceeding 1 ppb. The maximum concentration was recorded at 3.04 ppb (5-min data) at 11:09 local time of 13 July 2018. This



184 concentration of PAN is comparable to the levels recorded at downwind of Guangzhou, southern China (3.9 ppb) (Wang et al.,
185 2010), 2.51 ppb in Nashville, U.S (Roberts et al., 2002). However, this value was significantly lower than heavily polluted areas in
186 northern China in the summer, such as Beijing (9.34 ppb, (Xue et al., 2014)), Lanzhou (9.12 ppb, (Zhang et al., 2009)), and Jinan
187 (13.47 ppb, (Liu et al., 2018)). This is likely because the higher summer temperatures in the southeastern coastal region are
188 conducive to the thermal decomposition of PAN, and the precursor concentration of PAN is significantly lower than in the
189 northern region. Throughout the observation period, the variations in O₃ and PAN were almost identical, but the maximum
190 concentration of O₃ occurred at 3:00 p.m. on July 29th (114.12 ppb). The correlation between the daily maximum values of PAN
191 and BC is the strongest (R=0.85), followed by O₃ (R=0.75), suggesting that summertime haze and photochemical pollution were
192 deeply connected.



193
194 **Figure 1.** Time series of trace gases and meteorological parameters observed at IUE during 10-31 July 2018. The gray shading
195 represents days when the PM_{2.5} hourly daily maximum value exceeded 35 µg·m⁻³.

196

197 We categorize it as "haze" and "clean" based on whether the PM_{2.5} hourly daily maximum value is greater than 35 µg·m⁻³.



198 Specifically, "haze" includes July 11th, 13th, 21st to 23rd, and 25th to 31st, while other days are categorized as 'clean'. To provide
199 a quantitative perspective, the statistics for PAN and associated species were calculated and compiled in Table 1. PM_{2.5}
200 concentrations during the haze period were significantly higher than during the clean period, being 2.49 times that of the clean
201 period. There was no significant difference of UV levels between clean and haze periods, while temperatures in the haze phase
202 were notably higher than those in the clean phase. Therefore, without considering precursors, PAN concentrations should be
203 lower during the haze phase due to higher thermal decomposition. In fact, PAN concentrations during the haze period were 2.35
204 times higher than those during the clean period. During the haze period, ozone concentrations were also significantly higher than
205 during the clean period, being 2.04 times that of the clean period. These observations indicate that the atmospheric oxidation
206 capacity is relatively strong during the haze period. Similar to PAN, HONO also exhibits higher concentrations during the haze
207 phase (approximately 2.33 times that of clean conditions), which is consistent with current research findings that particles
208 promote the generation of HONO (Ye et al., 2017). NO also experienced an increase from clean (3.28 ppb) to hazy (4.30 ppb)
209 conditions, albeit less prominently than NO₂ (from 7.21 to 14.55 ppb). This observation further underscores that, during hazy
210 periods, the atmosphere demonstrates heightened oxidizing potential, facilitating the conversion of NO to NO₂. While the
211 increased NO levels on hazy days reduced PA radicals and hindered PAN formation, this effect was offset by the concurrently
212 higher concentrations of PAN precursors (NO₂ and VOCs) during those days. The TVOCs have increased to some extent, but in
213 hazy conditions, they are only 1.34 times that of clean conditions. This is also because the strong oxidizing conditions during
214 haze periods convert VOCs into secondary pollutants, such as O₃ and PAN. The TVOC levels at this site are comparable to that
215 at a rural site in a coastal city-Qingdao (7.6 ppb), significantly lower than inland sites (such as Wuhan (30.2, (Liu et al., 2021a))
216 and Chengdu (28.0 ppb, (Yang et al., 2020))) or economically more developed coastal cities (such as Shanghai (25.3 ppb, (Zhu et
217 al., 2020)) and Hong Kong (26.9, (Wang et al., 2018))), and significantly higher than regional background locations like Mt.
218 Wuyi (4.7 ppb, (Hong et al., 2019)), Mt. Waliguan (2.6 ppb, (Xue et al., 2013)), and Mt. Nanling (4.7 ppb, (Wang et al., 2023)).
219 The isoprene level during haze period was significantly higher than that during clean period probably due to haze period with
220 higher temperature (Wang et al., 2023). The wind speed was very low during both the clean and haze periods, especially during
221 the haze period with only 1.12 m·s⁻¹. The relative humidity was high during both periods, and there was no significant difference
222 between the clean and haze periods.

223 **Table 1.** Descriptive statistics of major trace gases (ppb), particulate matter (µg·m⁻³) and meteorological parameters during 10-31
224 July 2018.

Species	Clean (mean ± SD)	Haze (mean ± SD)
PAN	0.20 ± 0.23	0.47 ± 0.46***
O ₃	16.07 ± 12.73	32.79 ± 29.73***
HONO	0.27 ± 0.18	0.63 ± 0.43***
NO	3.28 ± 4.03	4.30 ± 8.39***



NO ₂	7.21 ± 3.87	14.55 ± 8.89***
TVOCs	6.13 ± 1.73	8.19 ± 2.55***
C ₃ H ₈	0.13 ± 0.04	0.17 ± 0.05***
PM ₁	10.13 ± 3.91	24.36 ± 10.77***
PM _{2.5}	11.21 ± 5.33	27.93 ± 13.16***
PM ₁₀	24.26 ± 9.45	47.28 ± 20.63***
UV (W·m ⁻²)	14.29 ± 17.38	13.18 ± 17.40
T (°C)	30.68 ± 2.39	31.92 ± 3.36***
RH (%)	81.94 ± 8.60	77.18 ± 8.22
WS (m·s ⁻¹)	1.64 ± 0.69	1.12 ± 0.61*

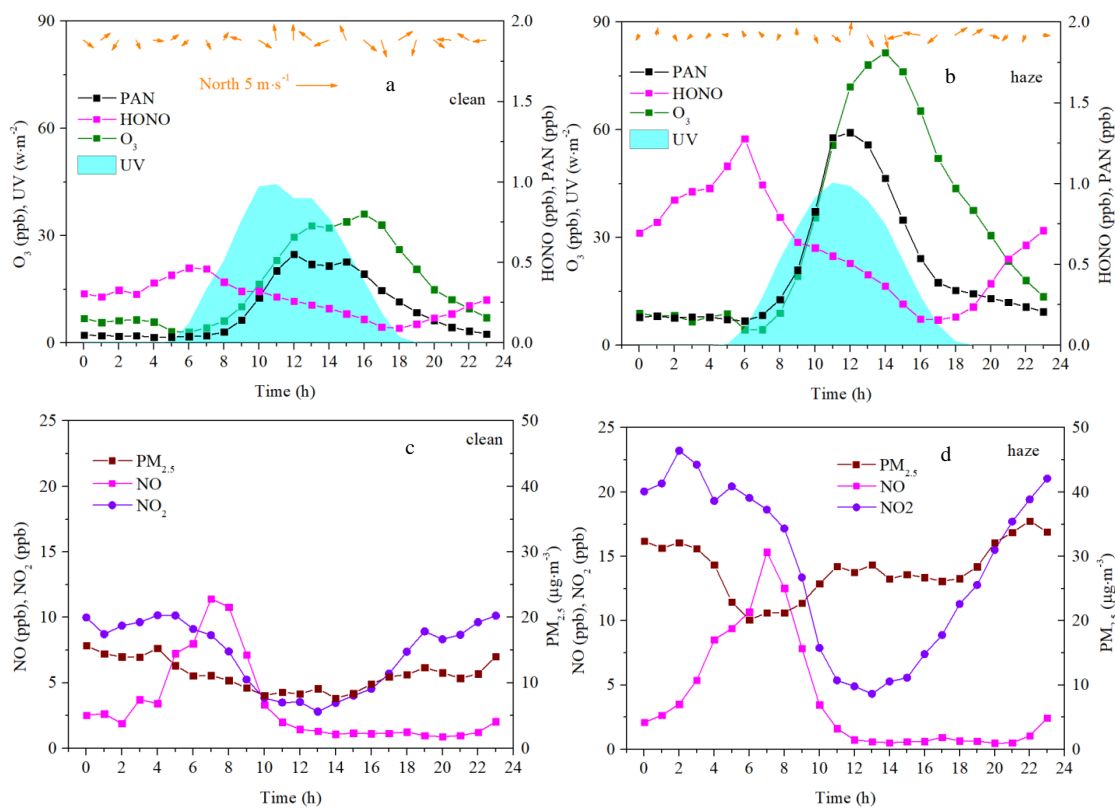
225 Note: *, **, and *** indicate that they passed the significance test at 0.05, 0.01 and 0.001 levels, respectively.

226

227 The average diurnal patterns of PAN and related variables have been averaged separately for clean and hazy conditions. The
228 daily variation of PAN exhibits a clear unimodal pattern, with concentrations starting to rise after sunrise and decreasing after
229 12:00 caused by thermal decomposition of PAN at high temperatures. The peak occurring at noon indicates that PAN primarily
230 originates locally, as a delay of about 1-2 hours would be expected if it were influenced by transportation (Liu et al., 2024). The
231 daytime increment was much larger for hazy condition (1.17 ppb) than for clean condition (0.52 ppb), indicating stronger
232 photochemical production of PAN for hazy condition. The daily variation pattern of ozone is similar to PAN, except that ozone
233 reaches its peak relatively later compared to PAN, with the peak occurring at 16:00 during the clean phase and 14:00 during the
234 haze phase. Although PAN and O₃ are both products of photochemical reactions involving NO_x and VOCs, their production
235 efficiencies differ. PAN is specifically formed from VOCs that are precursors to the acetyl radical (CH₃CO), whereas O₃ can be
236 produced from the oxidation of any VOCs. Analyzing the correlation between PAN and O₃ can offer insights into their respective
237 photochemical production efficiencies. As shown in Fig. S5, the positive correlation between the daily maximum values of PAN
238 and O₃ for clean condition (R²=0.6701) was better than that for hazy condition (R²=0.1504). The slopes of the linear regression
239 were 0.021 ppb/ppb for clean conditions and 0.009 for hazy conditions. This indicates that, on average, approximately 2.1 ppb of
240 PAN could be produced for each 100 ppb of O₃ formed under clean conditions, and about 0.9 ppb of PAN for each 100 ppb of O₃
241 under hazy conditions in the air masses reaching IUE. The slope of linear regression for clean condition is comparable to those
242 determined in Hongkong (0.028, (Xu et al., 2015)), Mexico (0.02, (Marley et al., 2007a)), and Nashville (0.025, (Roberts et al.,
243 2002)). The lower efficiency of PAN production relative to O₃ indicates that PAN precursors represent only a small portion of the
244 total VOCs, especially during hazy conditions. Additionally, the high temperatures in the southeast coastal region likely
245 contribute to the lower production efficiency of PAN. This result is consistent with the result that RIR during the cleaning period
246 is higher than that during the haze period. As shown in Fig. S6, in the clean period, the correlation between PAN and O₃ is the
247 strongest (R²=0.7042), indicating that O₃ and PAN are both photochemical end products during clean periods. In contrast, during
248 hazy periods, the correlation between PAN and O₃×JO¹D is the strongest (R²=0.6597), suggesting that O₃ plays a more



249 significant role in promoting PAN formation through photolysis to generate OH during hazy periods.
250 Unlike the daily variation patterns of PAN and O₃, HONO exhibits a swift concentration decrease after sunrise in both clean and
251 hazy conditions, undergoing photolytic conversion into OH radicals. Subsequently, in clean conditions, HONO starts to increase
252 in concentration after sunset. In hazy conditions, however, the increase begins from 16:00 LT and not after sunrise. This suggests
253 a robust daytime net production or transport of HONO, where the rates surpass those of HONO photolysis and other sinks in the
254 afternoon in hazy conditions. The NO levels reach their peak at 7:00 during the morning rush hour, reflecting advection of fresh
255 urban plumes to the study site. The daily variation of NO₂ exhibits a 'U' shape, reaching its minimum value at 13:00, mainly
256 owing to effects of emission, boundary layer height and photochemical reactions. In the clean period, the daily variation of PM_{2.5}
257 is similar to that of NO₂, both showing a 'U' shape, reaching their lowest values at noon. However, during the haze phase, the
258 daily variation pattern of PM_{2.5} appears somewhat different. There is a noticeable trough in the early morning, remains stable
259 during the day, and starts to rise after sunset.



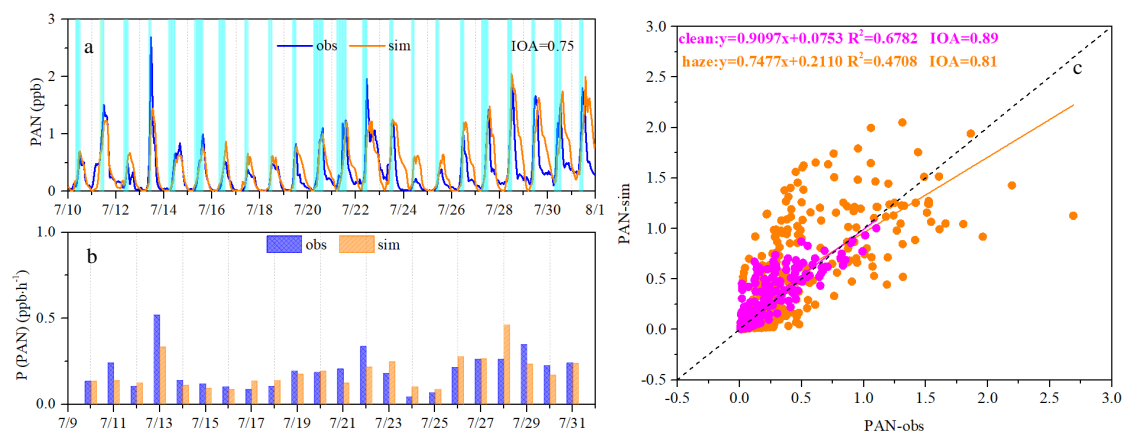
261
262 **Figure 2.** The diurnal variations of PAN, HONO, O₃, and UV during clean (a) and hazy (b) periods, as well as the diurnal
263 variations of PM_{2.5}, NO, and NO₂ during clean (c) and hazy (d) periods.

264

265 3.2 PAN formation: key factors and mechanisms



266 To investigate the key factors and mechanisms of PAN formation, PAN was simulated by constraining the MCM-based box
267 model with meteorological conditions and observed concentrations of precursor gases. The model successfully replicated the
268 variations in PAN, achieving an IOA of 0.75. (Fig. 3(a)), which was within the accepted range (0.66-0.87) in previous studies
269 (Zeng et al., 2019). The model captured its formation rate well in general, with observed rates varying from 0.04 to 0.52 ppb·h⁻¹
270 (average: 0.20 ppb·h⁻¹) and modeled rates ranging from 0.09 to 0.46 ppb·h⁻¹ (average: 0.19 ppb·h⁻¹) (see Fig. 3(b)). The similar
271 result was found in the North China Plain (NCP) region in the wintertime (Xu et al., 2021). When calculating the IOA separately
272 for clean and hazy periods, it was found that the IOA significantly increased to 0.89 and 0.81 (Fig. 3(c)), respectively. This
273 phenomenon indicates a substantial difference in the PAN production and destruction mechanisms between clean and hazy
274 periods. Furthermore, the simulated values are closer to the observed values during clean period, reflected in a higher R² value
275 (R²=0.6782) and a K value closer to 1 (K=0.9097) (Fig. 3(c)). In contrast, the R² value and the K value during hazy period are
276 only 0.4708 and 0.7477, respectively (Fig. 3(c)). This phenomenon suggests that reactions without considered in MCM may
277 enhance PAN generation during hazy periods.

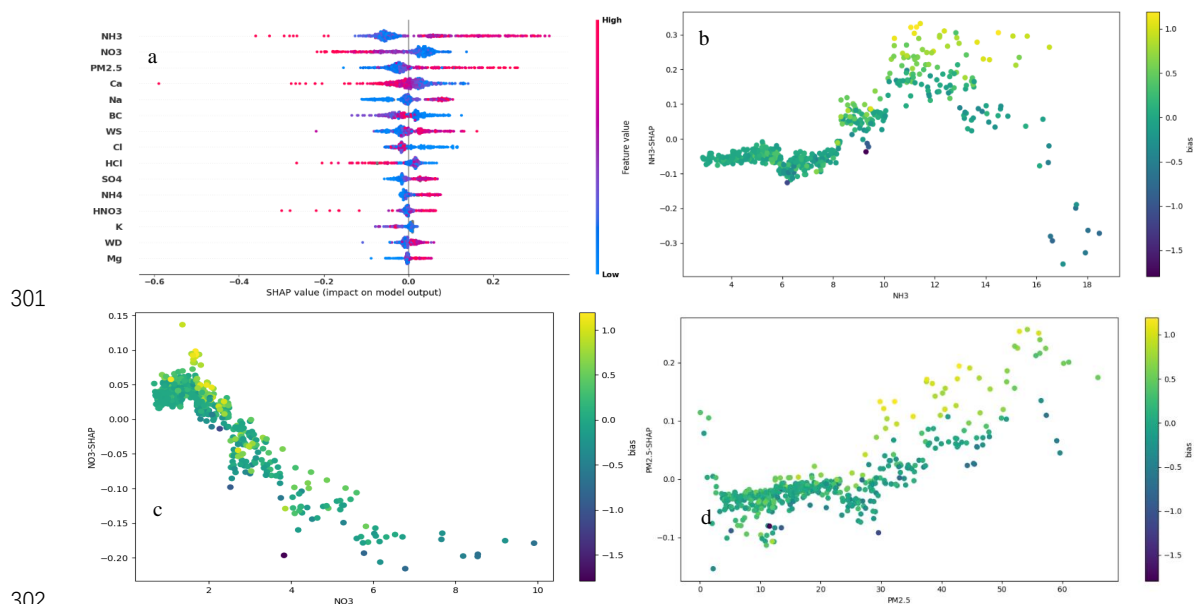


278
279 **Figure 3.** Comparisons of modeled PAN and observed PAN (a) variation (daytime photochemical PAN production periods
280 indicated by cyan shading), (b) production rates, (c) correlation between PAN observations and simulated values

281
282 To identify the key factors influencing the performance of the model simulation, we used the difference between the model
283 simulation values and the observed values (bias) as the target. The remaining variables, which were not input into the OBM
284 model, such as NH₃, HNO₃, HCl (alkaline and acidic gaseous pollutants), PM_{2.5} concentrations and their components, as well as
285 physical process parameters like wind speed and wind direction, were used as features. As shown in Fig. 4 (a), through
286 XGBoost-SHAP machine learning, we found that NH₃ is the most significant parameter affecting bias, contributing 19.68 %. A
287 scatter plot analysis of the SHAP values of NH₃ versus NH₃ concentrations revealed that as NH₃ concentrations increase (Fig. 4
288 (b)), the OBM model tends to overestimate more significantly. To date, there are very few studies that directly address the impact
289 of NH₃ on PAN formation. Xu et al. (2021) suggested that NH₃ could promote the formation of HONO, which in turn affects



290 PAN formation. However, since we included HONO as an input to constrain the model, the indirect influence of NH_3 on PAN
291 formation through HONO can be excluded. NH_3 in the atmosphere can preferentially react with sulfuric acid (H_2SO_4) to form
292 ammonium sulfate ($(\text{NH}_4)_2\text{SO}_4$) secondary inorganic aerosols (Behera et al., 2013), leading to the heterogeneous reaction
293 removal of PAN by secondary inorganic aerosols. This result is validated by the negative correlation between the SHAP values
294 of NH_4^+ and SO_4^{2-} and their respective concentrations. NO_3^- is the second most significant parameter influencing the bias
295 between the two, contributing 11.33 % (Fig. 4 (a)). NO_3^- has a negative correlation with the bias (Fig. 4 (c)), indicating that
296 higher NO_3^- levels lead to more significant underestimation by the model, suggesting that NO_3^- promotes PAN formation in the
297 actual atmosphere (Hanst, 1971). $\text{PM}_{2.5}$ is the third most significant parameter (Fig. 4 (a)), contributing 9.4 %. $\text{PM}_{2.5}$ has a
298 positive correlation with the bias (Fig. 4 (d)), indicating that higher $\text{PM}_{2.5}$ levels lead to more significant overestimation by the
299 model, suggesting that PAN can undergo heterogeneous removal on the surface of $\text{PM}_{2.5}$ in the actual atmosphere (Sun et al.,
300 2022).



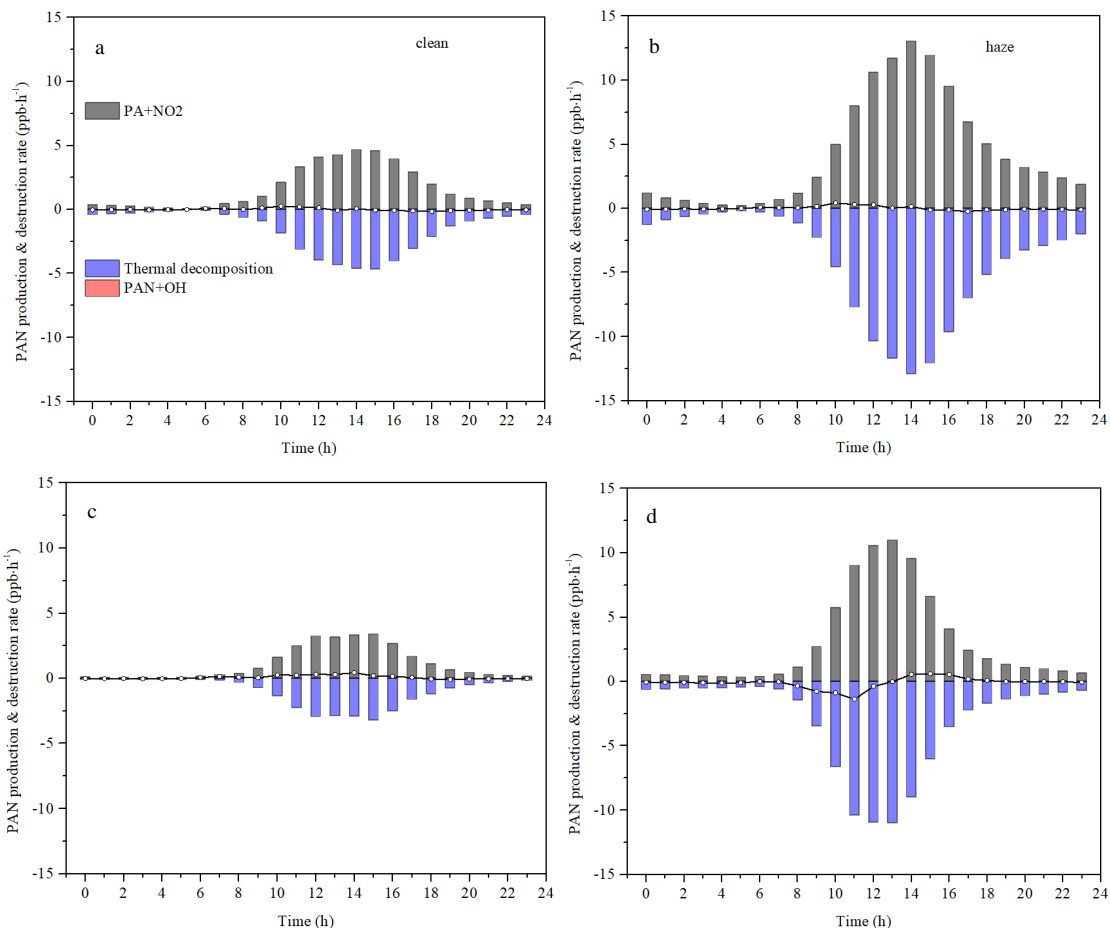
301
302
303 **Figure 4.** Feature importance was obtained by XGBoost-SHAP method (a). The scatter plots between concentration of top three
304 important features and their SHAP values (b-d), and colored with the difference between the model simulation values and the
305 observed values (bias).

306
307 Figure 5 (a) and (b) show the average production and destruction rates of PAN during clean and haze periods without PAN
308 constrained. During the haze period, both the production and destruction rates of PAN are significantly higher than during the
309 clean period. The higher production rate of PAN during the haze period is due to the higher concentration of PAN precursors,
310 while the higher destruction rate is because both the temperature and PAN concentration are higher. Regarding the net



311 production rate, it is also higher during the haze period than during the clean period, which corresponds to the previously
312 observed diurnal variation. From 6:00 to 12:00 during the haze period, the net production rate of PAN is positive, with an
313 average value of $0.19 \text{ ppb}\cdot\text{h}^{-1}$. During the clean period, from 6:00 to 12:00, the net production rate of PAN is $0.12 \text{ ppb}\cdot\text{h}^{-1}$. The
314 diurnal variation of PAN shows that from 6:00 to 12:00, the average net production rates during the haze and clean periods are
315 $0.20 \text{ ppb}\cdot\text{h}^{-1}$ and $0.09 \text{ ppb}\cdot\text{h}^{-1}$, respectively. The model-simulated net production rate is close to the observed net production rate,
316 further indicating that the model can simulate PAN well, and also confirming that PAN in summer mainly comes from local
317 production. The net production rate of PAN during the haze period is similar to the summer results in urban areas of the Pearl
318 River Delta (PRD), which is $0.17 \text{ ppb}\cdot\text{h}^{-1}$, while the net production rate of PAN during the clean period is similar to the summer
319 results in rural areas of the PRD, which is $0.12 \text{ ppb}\cdot\text{h}^{-1}$ (Liu et al., 2024).

320 Figure 5 (c) and (d) show the average production and destruction rates of PAN during clean and haze periods with PAN
321 constrained. The net production rate of PAN is approximately zero at night during both clean and haze periods, while there is a
322 significant difference in the net production rate during the day. During the clean period, the daytime net production rate of PAN is
323 greater than zero, with an average value of $0.19 \text{ ppb}\cdot\text{h}^{-1}$. In contrast, during the haze period, the net production rate of PAN is
324 negative from 6 a.m. to 1 p.m., with an average value of $-0.47 \text{ ppb}\cdot\text{h}^{-1}$, and positive from 2 p.m. to 5 p.m., with an average value
325 of $0.47 \text{ ppb}\cdot\text{h}^{-1}$. Previous research has shown that an increase in temperature, an increase in PAN concentration, or a decrease in
326 PAN precursors (including VOCs and NO_2) can cause the net production rate of PAN to change from positive to negative (Liu et
327 al., 2024). We conducted a correlation analysis of the net production rate of PAN with temperature, PAN concentration, VOCs,
328 and NO_2 and found that the net production rate of PAN had the best correlation with PAN concentration ($R^2=0.1316$), showing a
329 significant negative correlation ($k=-0.5283$) (Fig. S7). Additionally, we also observed that when the net production rate of PAN is
330 negative, the PAN concentration is often very high (Fig. S7). As shown in Fig. 5, we conducted sensitivity experiments by
331 reducing the PAN concentration by 80 %, i.e., 0.2 times the observed value, and found that the net production rate of PAN was
332 positive throughout the observation period. Conversely, when the PAN concentration was increased by 140%, i.e., 2.4 times the
333 observed value, the net production rate of PAN was found to be almost negative throughout the observation period. Besides, we
334 also conducted sensitivity experiments on temperature and found that when simulating winter temperatures, i.e., 0.4 times the
335 observed value, with a temperature range of $9.25\text{-}15.29^\circ\text{C}$, the net production rate of PAN was positive throughout the observation
336 period. Similarly, when simulating spring and autumn temperatures, i.e., 0.6 times the observed value, with a temperature range of
337 $13.87\text{-}23.39^\circ\text{C}$, the net production rate of PAN was also positive throughout the observation period. In conclusion, the net
338 production rate of PAN becomes negative with PAN constrained, further suggesting the existence of an unknown compensatory
339 mechanism.

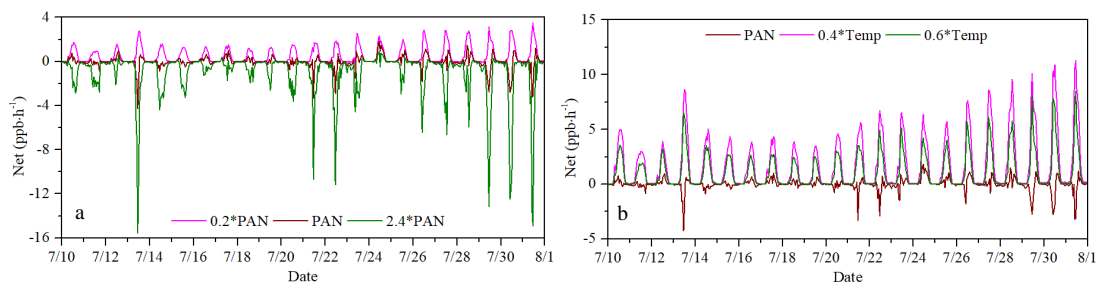


340

341

342 **Figure 5.** Average diurnal variation of the simulated production, destruction and net rates of PAN during clean (a) and haze (b)
 343 without PAN constrained. And average diurnal variation of the simulated production, destruction and net rates of PAN during
 344 clean (c) and haze (d) with PAN constrained.

345



346

347 **Figure 6.** Net PAN production rates at different PAN concentrations (a) and different temperatures (b)

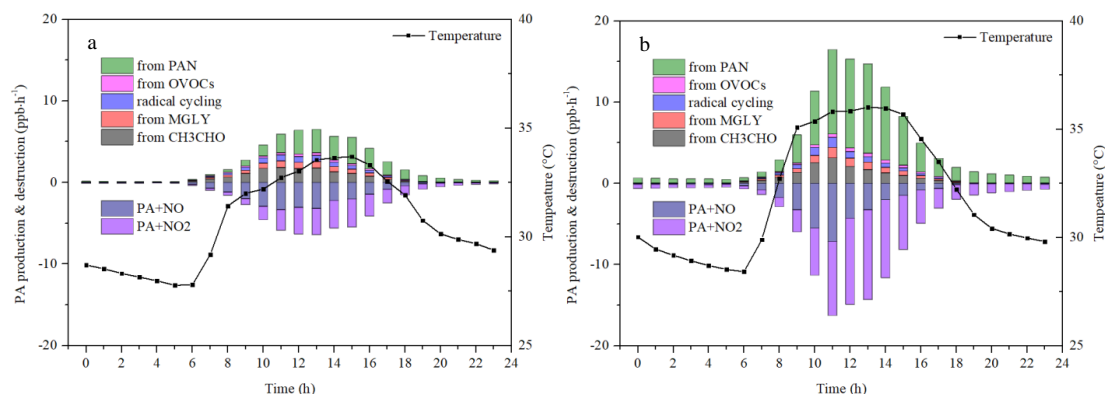
348

349 PAN is formed when the PA radical reacts with NO₂. Given the swift equilibrium between R2 and R4 at high temperatures, budget



350 analysis of PA's production and consumption pathways is frequently used to detail the mechanisms behind PAN formation (Sun et
351 al., 2020). Figure 7 illustrates the diurnal patterns of the primary production and loss pathways for the PA radical across different
352 periods. As shown in Fig. 7, during haze days, the rates of PA production and destruction were twice as high as those on clean
353 days. This indicates that radical cycling and photochemical formation were more efficient during haze days, driven by higher
354 temperatures and a greater abundance of precursors (Zeng et al., 2019). The PA radical production rate from PAN thermal
355 decomposition reached its peak at 15:00 (3.22 ppb-h⁻¹) and 13:00 (10.99 ppb-h⁻¹) for clean and haze days, perfectly coinciding
356 with the peak temperature time. In addition, the conversion of PAN into PA radical through thermal decomposition had high
357 correlations with temperature during both haze ($R^2=0.82$) and clean days ($R^2=0.77$). The conversion of PAN into PA radical
358 through thermal decomposition during haze days was significantly higher than that during clean days, which was not only
359 enhanced by higher temperature but also maintained by higher PAN concentration during haze days. The thermal decomposition
360 of PAN to PA radical during the day (5:00-18:00 local time) accounted for 68.22 % and 45.59 % during haze and clean days,
361 respectively. The pathways that did not account for the transformation between PA and PAN reached their peak around noon
362 (11:00 local time), coinciding with the highest solar radiation and the most intense photochemical reactions, which has been
363 observed in spring and autumn at the same site (Liu et al., 2022).

364 Production rates of PA from other pathways related to precursors showed single-peak patterns of these four pathways around noon,
365 which suggested that the PA radical generated from these pathways was primarily increased by intense solar radiation at noontime
366 (Sun et al., 2020). The average day PA radical production rates from CH₃CHO via reactions with OH and NO₃ were 1.10 and 0.93
367 ppb-h⁻¹, accounting for 48.85% and 49.35 % (exclude PAN thermal decomposition sources) during haze and clean days,
368 respectively. These percentages were comparable to previous studies in Guangzhou (46 %) (Yuan et al., 2018) and Beijing (34.11-
369 50.19 %) (Xue et al., 2014), suburban site of Chongqing (47.72 %) (Sun et al., 2020). The second production pathway involved
370 MGLY undergoing photolysis and oxidation through reactions with OH and NO₃ (haze: 0.50 ppb-h⁻¹ and clean: 0.42 ppb-h⁻¹),
371 contributing to 22.27 % and 22.12 % for haze and clean days, respectively. Subsequently, radical cycling processes—including the
372 decomposition of RO radicals and the reactions of acyl peroxy radicals with NO—were also significant contributors to PA
373 production, accounting for 18.98% on haze days and 19.54% on clean days. PA from the other OVOCs (excluding CH₃CHO,
374 MGLY) via photolysis and oxidation reactions involving OH, NO₃, and O₃, accounted for 9.90 % and 8.99% during haze (0.22
375 ppb-h⁻¹) and clean days (0.17 ppb-h⁻¹). There were no notable differences in the proportions of individual pathways contributing to
376 PA between haze and clean days, indicating comparable pollutant compositions in the atmospheric around IUE (Zeng et al., 2019).
377 The primary contributor to the PAN destruction rate was the reaction between PA and NO₂, accounting for 67.72 % and 51.09 %
378 during haze (4.74 ppb-h⁻¹) and clean days (1.76 ppb-h⁻¹), respectively, followed by PA+NO, contributing to 32.28 % and 48.91 %
379 during haze (2.26 ppb-h⁻¹) and clean days (1.69 ppb-h⁻¹), respectively.



380

381 **Figure 7.** PA radical production and destruction pathways on (a) clean days and (b) haze days.

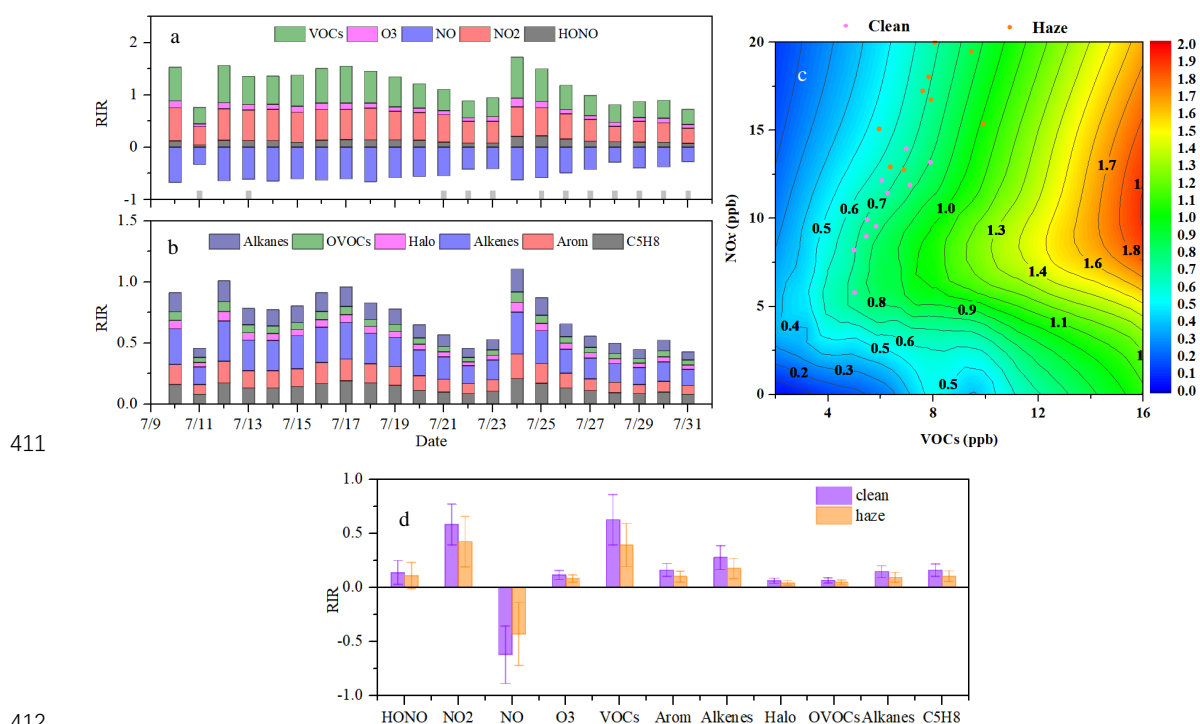
382

383 3.3 Sensitivity of PAN formation and its impact on the local atmosphere

384 To determine the principal precursors influencing PAN formation, sensitivity modeling analyses were carried out to investigate
385 how PAN relates to its precursors. The RIR reflects how sensitive PAN formation is to changes in its precursor levels. As shown
386 in Fig.8 (a), decreases in NO led to strong negative RIR ranging from -0.67 to -0.27 (-0.52 ± 0.13) throughout the observation
387 period. However, RIR is positive for other species, with NO₂ (0.50 ± 0.11) and VOCs (0.50 ± 0.15) having the highest RIR,
388 followed by HONO (0.12 ± 0.04) and O₃ (0.10 ± 0.03). Around 50 types of VOCs were classified as alkanes, OVOCs,
389 halogenated hydrocarbons (Halo), alkenes, aromatics (Arom), and isoprene (C₅H₈ representing biogenic hydrocarbons). Among
390 these VOCs, the RIR of alkenes (0.22 ± 0.07) is the highest, followed by C₅H₈ (0.13 ± 0.04) and Arom (0.13 ± 0.04), while
391 OVOCs (0.06 ± 0.01) and Halo (0.05 ± 0.01) have very low RIRs (Fig. 8 (b)). These phenomena indicated that increased NO
392 level would inhibit the production of PAN while increased NO₂, VOCs (especially alkenes, C₅H₈, and Arom), HONO, and O₃
393 would promote the production of PAN. Because the values of NO and NO₂ RIR are approximately equal but with opposite signs,
394 the RIR for NO_x is almost zero, indicating that the PAN generation at this site is not sensitive to NO_x. Zeng et al. (2019) also
395 observed that NO₂ had a positive effect on PAN formation, while NO had a negative effect, in a suburban area of Hong Kong.
396 This finding aligns with the fact that NO₂ directly contributes to PAN production, whereas NO reduces PA radicals, thereby
397 inhibiting PAN formation. Based on the scenario analysis (Empirical Kinetic Modeling Approach (EKMA)), all data points for
398 the 22 days fell above the ridge line (Fig. 8(c)). A reduction in VOCs at these points resulted in lower PAN concentrations,
399 indicating that PAN formation at IUE was influenced by VOCs and thus VOC-sensitive. Our previous research also found that in
400 this coastal city, PAN generation is limited by VOCs during the spring and autumn seasons. The difference is that previous
401 studies indicated that reducing NO₂, like reducing NO, also leads to an increase in PAN concentration in spring and autumn (Liu
402 et al., 2022). This is because the NO_x concentration in spring and autumn is significantly higher than in summer, which is
403 consistent with that both NO₂ and NO inhibit the formation of PAN in regions with high NO_x concentrations (Liu et al., 2024).



404 We divided the RIRs for different species into haze and clean periods and found that the RIRs during clean periods were
405 consistently higher than those during haze periods (Fig. 8(d)), which indicated that altering the concentrations of these species
406 during clean periods had a greater impact on PAN formation. The rapid thermal decomposition of PAN at high temperatures is
407 likely the primary reason. During the haze period, the main source of PA radical was PAN decomposition, which accounted for
408 68.22%, and the other sources were smaller than that during the clean period (the source of the PA radical would be demonstrated
409 in the following paragraph). Therefore, the sensitivity of PAN production to precursors and HONO & O₃ producing OH became
410 lower during the haze period (Liu et al., 2021b; Liu et al., 2022).



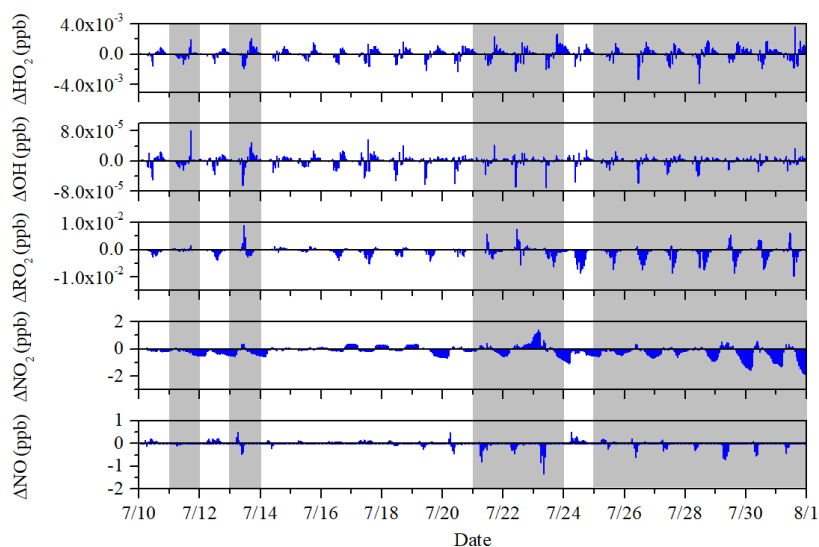
412
413 **Figure 8.** These four figures illustrate the RIR of PAN formation to major precursors (a), the impact of different VOCs species (b),
414 the isopleth diagrams of PAN formation (c), and a comparison of RIRs between clean and polluted periods (d).

415

416 As shown in Fig. 9, ΔHO_2 and ΔOH are positive for most periods, indicating that the PAN mechanism promotes the generation of
417 HO_2 and OH. Over the entire period, ΔHO_2 is 8.43×10^{-5} ppb, with no significant difference between clean and hazy periods, being
418 8.18×10^{-5} ppb and 8.64×10^{-5} ppb respectively. OH behaves similarly, with ΔOH being 4.55×10^{-7} ppb over the entire period, and
419 also showing no significant difference between clean and hazy periods, being 4.93×10^{-7} ppb and 4.23×10^{-7} ppb respectively. The
420 increase in simulated OH and HO_2 concentrations suggests that PAN photochemistry is enhancing radical formation and AOC at
421 this site (Liu et al., 2024). Unlike HO_2 and OH, ΔRO_2 , ΔNO_2 , and ΔNO are negative for most periods, because PAN formation
422 uses up PA and NO_2 , the reduction in PA leads to a decrease in the amount of RO_2 . Over the entire period, ΔRO_2 is -6.4×10^{-4} ppb,

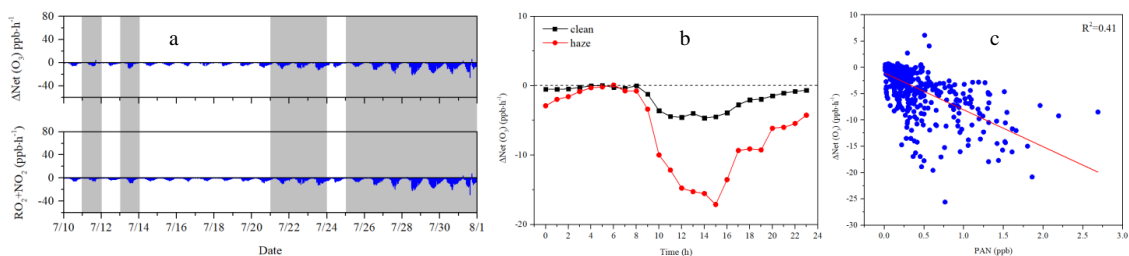


423 with no significant difference between clean and hazy periods, being -6.1×10^{-4} ppb and -6.5×10^{-4} ppb respectively. The average
424 values of ΔNO_2 and ΔNO during the entire observation period are -0.17 and -0.01 ppb respectively, with significant differences
425 between hazy and clean periods. Specifically, ΔNO_2 is -0.22 during hazy periods and only -0.11 during clean periods, indicating
426 that the PAN mechanism consumes more NO_2 during hazy periods. Similarly, ΔNO is -0.05 during hazy periods, showing an
427 inhibitory effect, while it is 0.03 during clean periods, showing a promoting effect.



428
429 **Figure 9.** The difference of HO_2 , OH , RO_2 , NO_2 , and NO between base scenario with PAN mechanism and scenario without PAN
430 mechanism

431
432 As shown in Fig.10 (a), the PAN mechanism inhibited 85.80% of net ozone production during the entire observation period, with
433 inhibition rates of 83.75% and 87.50% during clean and haze periods, respectively. This result is consistent with previous spring
434 observations at the same site, where the inhibition rate was 83% (Liu et al., 2022). The PAN mechanism mainly inhibits the net
435 ozone generation by increasing the RO_2+NO_2 reaction (Fig.10(a)), with negligible impact from other reactions (Fig. S11). As
436 shown in Fig.10(b), the diurnal variation trend indicates that the PAN mechanism's inhibitory effect on ozone is significantly
437 greater during haze periods than during clean periods. Additionally, regardless of whether it is during haze periods or clean
438 periods, the PAN mechanism's inhibitory effect on ozone is significantly greater during the day than at night. These phenomena all
439 indicate that the higher the PAN concentration, the more pronounced the inhibitory effect of the PAN mechanism on ozone
440 (Fig.10(c)). Under low precursor conditions, competition among these precursors may limit their secondary formation, thus
441 resulting in inhibition (Liu et al., 2024).



442

443 **Figure 10.** (a) Time series plot of $\Delta\text{Net}(\text{O}_3)$ and the reaction of RO_2+NO_2 , (b) Diurnal variation of $\Delta\text{Net}(\text{O}_3)$ during clean and
444 hazy conditions, (c) Correlation between $\Delta\text{Net}(\text{O}_3)$ and PAN.

445

446 **Conclusion**

447 This study thoroughly investigated the summertime PAN formation mechanism and established its connection to haze pollution. In
448 addition to NO and TVOCs, the concentration of all pollutants during the haze period is above twice that during the cleaning
449 period, indicating that the oxidation of NO and TVOCs during the haze period is stronger, which is conducive to the oxidation of
450 NO and TVOCs into secondary pollutants, such as O_3 and PAN. The slopes of linear regression between the daily maximum
451 values of PAN and O_3 were 0.021 ppb/ppb and 0.009 for clean and hazy condition, respectively, implies that PAN precursors
452 accounted for only a small fraction of the total VOCs, especially for hazy condition. High temperature should be another factor
453 contributing to the lower production efficiency of PAN in the southeast coastal region. During the whole observation period, the
454 IOA=0.75, indicating that the MCM model is well-suited for exploring the photochemical formation of PAN. During the clean
455 period, simulation results were better than during the haze period (R^2 : 0.6782 vs. 0.4708, slope K: 0.9097 vs. 0.7477), indicating
456 that PAN during the haze period may originate from reactions without considered in MCM. Additionally, the net production rate
457 of PAN becomes negative with PAN constrained. This further indicates that, despite the high temperatures, there is still a
458 significant concentration of PAN, suggesting the existence of an unknown compensatory mechanism. Through XGBoost-SHAP
459 machine learning, this unknown compensatory mechanism may involve NO_3^- promoting PAN formation. Both RIR and EKMA
460 indicate that PAN formation in this region is VOC-controlled. Controlling emissions of VOCs, particularly alkenes, C_5H_8 , and
461 aromatics, would be beneficial for mitigating PAN pollution. The RIR results also show that during the clean period, PAN is more
462 sensitive to changes in various pollutants than during the haze period, highlighting the significant importance of deep emission
463 reductions. PAN presented the promotion effects on OH and HO_2 , while inhibited O_3 formation, RO_2 , NO and NO_2 . This study
464 improves our thorough understanding of PAN photochemistry and offers valuable scientific guidance for the future management
465 of PAN pollution.

466



467 **Data availability**

468 The observation data at this site are available from the authors upon request.

469 **Authorship Contribution Statement**

470 **Baoye Hu:** Methodology, Formal analysis, Investigation, Data curation, Writing – original draft. **Naihua Chen:** Software, Formal
471 analysis. **Rui Li:** Software, Formal analysis. **Mingqiang Huang:** Software. **Jinsheng Chen:** Funding acquisition, Supervision,
472 Writing - Review & Editing. **Youwei Hong:** Formal analysis. **Lingling Xu:** Investigation. Xiaolong Fan: Investigation. **Mengren**
473 **Li:** Investigation. **Lei Tong:** Investigation. **Qiuping Zheng:** Investigation. **Yuxiang Yang:** Writing - Review & Editing

474 **Competing interests**

475 The authors declare that they have no conflict of interest.

476 **Acknowledgments**

477 This work was supported by the National Natural Science Foundation of China (grant nos. 42305102, U22A20578), Natural
478 Science Foundation of Fujian Province (grant nos. 2023J05179), Natural Science Foundation of Zhangzhou City (grant nos.
479 ZZZ2023J07), Fujian Provincial Department of Education (grant nos. JAT210279), the Fund of Minnan Normal University
480 President (grant nos. KJ2021009). This study was funded by Xiamen Atmospheric Environment Observation and Research Station
481 of Fujian Province, and Fujian Key Laboratory of Atmospheric Ozone Pollution Prevention (Institute of Urban Environment,
482 Chinese Academy of Sciences).

483 **Supplementary information**

484 Attached please find supplementary information associated with this article.

485 **Reference**

486 Behera, S. N., Sharma, M., Aneja, V. P., and Balasubramanian, R.: Ammonia in the atmosphere: a review on emission sources,
487 atmospheric chemistry and deposition on terrestrial bodies, Environ. Sci. Pollut. Res., 20, 8092-8131, 10.1007/s11356-013-
488 2051-9, 2013.
489 Duan, J., Qin, M., Ouyang, B., Fang, W., Li, X., Lu, K., Tang, K., Liang, S., Meng, F., Hu, Z., Xie, P., Liu, W., and Häseler, R.:



- 490 Development of an incoherent broadband cavity-enhanced absorption spectrometer for in situ measurements of HONO and
491 NO₂, *Atmos. Meas. Tech.*, 11, 4531-4543, 10.5194/amt-11-4531-2018, 2018.
- 492 Hanst, P. L.: Mechanism of Peroxyacetyl Nitrate Formation, *J. Air Pollut. Control Assoc.*, 21, 269-271,
493 10.1080/00022470.1971.10469527, 1971.
- 494 Hong, Z., Li, M., Wang, H., Xu, L., Hong, Y., Chen, J., Chen, J., Zhang, H., Zhang, Y., Wu, X., Hu, B., and Li, M.: Characteristics
495 of atmospheric volatile organic compounds (VOCs) at a mountainous forest site and two urban sites in the southeast of China,
496 *Sci. Total Environ.*, 657, 1491-1500, 10.1016/j.scitotenv.2018.12.132, 2019.
- 497 Hu, B., Liu, T., Hong, Y., Xu, L., Li, M., Wu, X., Wang, H., Chen, J., and Chen, J.: Characteristics of peroxyacetyl nitrate (PAN)
498 in a coastal city of southeastern China: Photochemical mechanism and pollution process, *Sci. Total Environ.*, 719,
499 10.1016/j.scitotenv.2020.137493, 2020.
- 500 Hu, B., Wang, Y., Chen, J., Chen, N., Hong, Y., Xu, L., Fan, X., Li, M., and Tong, L.: The observation of atmospheric HONO by
501 wet-rotating-denuder ion chromatograph in a coastal city: Performance and influencing factors, *Environ. Pollut.*, 356,
502 10.1016/j.envpol.2024.124355, 2024.
- 503 Hu, B., Duan, J., Hong, Y., Xu, L., Li, M., Bian, Y., Qin, M., Fang, W., Xie, P., and Chen, J.: Exploration of the atmospheric
504 chemistry of nitrous acid in a coastal city of southeastern China: results from measurements across four seasons, *Atmos.*
505 *Chem. Phys.*, 22, 371-393, 10.5194/acp-22-371-2022, 2022.
- 506 Li, H., Yang, Y., Su, H., Wang, H., Wang, P., and Liao, H.: Ozone Pollution in China Affected by Climate Change in a Carbon
507 Neutral Future as Predicted by a Process-Based Interpretable Machine Learning Method, *Geophys. Res. Lett.*, 51,
508 10.1029/2024gl109520, 2024.
- 509 Liu, L., Wang, X., Chen, J., Xue, L., Wang, W., Wen, L., Li, D., and Chen, T.: Understanding unusually high levels of
510 peroxyacetyl nitrate (PAN) in winter in Urban Jinan, China, *J. Environ. Sci.*, 71, 249-260, 10.1016/j.jes.2018.05.015, 2018.
- 511 Liu, T., Chen, G., Chen, J., Xu, L., Li, M., Hong, Y., Chen, Y., Ji, X., Yang, C., Chen, Y., Huang, W., Huang, Q., and Wang, H.:
512 Seasonal characteristics of atmospheric peroxyacetyl nitrate (PAN) in a coastal city of Southeast China: Explanatory factors
513 and photochemical effects, *Atmos. Chem. Phys.*, 22, 4339-4353, 10.5194/acp-22-4339-2022, 2022.
- 514 Liu, T., Wang, Y., Cai, H., Wang, H., Zhang, C., Chen, J., Dai, Y., Zhao, W., Li, J., Gong, D., Chen, D., Zhai, Y., Zhou, Y., Liao, T.,
515 and Wang, B.: Complexities of peroxyacetyl nitrate photochemistry and its control strategies in contrasting environments in
516 the Pearl River Delta region, *Npj Clim. Atmos. Sci.*, 7, 10.1038/s41612-024-00669-3, 2024.
- 517 Liu, X., Guo, H., Zeng, L., Lyu, X., Wang, Y., Zeren, Y., Yang, J., Zhang, L., Zhao, S., Li, J., and Zhang, G.: Photochemical ozone
518 pollution in five Chinese megacities in summer 2018, *Sci. Total Environ.*, 801, 149603, 10.1016/j.scitotenv.2021.149603,
519 2021a.
- 520 Liu, Y., Shen, H., Mu, J., Li, H., Chen, T., Yang, J., Jiang, Y., Zhu, Y., Meng, H., Dong, C., Wang, W., and Xue, L.: Formation of



- 521 peroxyacetyl nitrate (PAN) and its impact on ozone production in the coastal atmosphere of Qingdao, North China, *Sci. Total*
522 *Environ.*, 778, 10.1016/j.scitotenv.2021.146265, 2021b.
- 523 Lu, X., Zhang, L., Wang, X., Gao, M., Li, K., Zhang, Y., Yue, X., and Zhang, Y.: Rapid Increases in Warm-Season Surface Ozone
524 and Resulting Health Impact in China Since 2013, *Environ. Sci. Tech. Lett.*, 7, 240-247, 10.1021/acs.estlett.0c00171, 2020.
- 525 Marley, N. A., Gaffney, J. S., Ramos-Villegas, R., and ´, B. C. G.: Comparison of measurements of peroxyacyl nitrates and
526 primary carbonaceous aerosol concentrations in Mexico City determined in 1997 and 2003, *Atmos. Chem. Phys.*, 7, 2277-
527 2285, 2007a.
- 528 Marley, N. A., Gaffney, J. S., Ramos-Villegas, R., and Gonzalez, B. C.: Comparison of measurements of peroxyacyl nitrates and
529 primary carbonaceous aerosol concentrations in Mexico City determined in 1997 and 2003, *Atmos. Chem. Phys.*, 7, 2277-
530 2285, 2007b.
- 531 Roberts, J. M., Flocke, F., Stroud, C. A., Hereid, D., Williams, E., Fehsenfeld, F., Brune, W., Martinez, M., and Harder, H.:
532 Ground-based measurements of peroxy-carboxylic nitric anhydrides (PANs) during the 1999 Southern Oxidants Study
533 Nashville Intensive, *J Geophys Res-Atmos*, 107, ACH 1-1-ACH 1-10, 10.1029/2001jd000947, 2002.
- 534 Sun, M., Cui, J. n., Zhao, X., and Zhang, J.: Impacts of precursors on peroxyacetyl nitrate (PAN) and relative formation of PAN to
535 ozone in a southwestern megacity of China, *Atmos. Environ.*, 231, 10.1016/j.atmosenv.2020.117542, 2020.
- 536 Sun, M., Zhou, Y., Wang, Y., Qiao, X., Wang, J., and Zhang, J.: Heterogeneous Reaction of Peroxyacetyl Nitrate on Real-World
537 PM_{2.5} Aerosols: Kinetics, Influencing Factors, and Atmospheric Implications, *Environ. Sci. Tech.*, 56, 9325-9334,
538 10.1021/acs.est.2c03050, 2022.
- 539 Taylor, O. C.: Importance of peroxyacetyl nitrate (PAN) as a phytotoxic air pollutant, *J. Air Pollut. Control Assoc.*, 19, 347-351,
540 10.1080/00022470.1969.10466498, 1969.
- 541 Wang, B., Shao, M., Roberts, J. M., Yang, G., Yang, F., Hu, M., Zeng, L., Zhang, Y., and Zhang, J.: Ground-based on-line
542 measurements of peroxyacetyl nitrate (PAN) and peroxypropionyl nitrate (PPN) in the Pearl River Delta, China. , *Int. J.*
543 *Environ. Anal. Chem.*, 90, 548-559, 10.1080/03067310903194972, 2010.
- 544 Wang, H., Lyu, X., Guo, H., Wang, Y., Zou, S., Ling, Z., Wang, X., Jiang, F., Zeren, Y., Pan, W., Huang, X., and Shen, J.: Ozone
545 pollution around a coastal region of South China Sea: interaction between marine and continental air, *Atmos. Chem. Phys.*,
546 18, 4277-4295, 10.5194/acp-18-4277-2018, 2018.
- 547 Wang, Y., Liu, T., Gong, D., Wang, H., Guo, H., Liao, M., Deng, S., Cai, H., and Wang, B.: Anthropogenic Pollutants Induce
548 Changes in Peroxyacetyl Nitrate Formation Intensity and Pathways in a Mountainous Background Atmosphere in Southern
549 China, *Environ. Sci. Tech.*, 10.1021/acs.est.2c02845, 2023.
- 550 Wu, X., Xu, L., Hong, Y., Chen, J., Qiu, Y., Hu, B., Hong, Z., Zhang, Y., Liu, T., Chen, Y., Bian, Y., Zhao, G., Chen, J., and Li, M.:
551 The air pollution governed by subtropical high in a coastal city in Southeast China: Formation processes and influencing



- 552 mechanisms, *Sci. Total Environ.*, 692, 1135-1145, 10.1016/j.scitotenv.2019.07.341, 2019.
- 553 Xu, W., Zhang, G., Wang, Y., Tong, S., Zhang, W., Ma, Z., Lin, W., Kuang, Y., Yin, L., and Xu, X.: Aerosol Promotes Peroxyacetyl
554 Nitrate Formation During Winter in the North China Plain, *Environ. Sci. Technol.*, 55, 3568-3581, 10.1021/acs.est.0c08157,
555 2021.
- 556 Xu, X., Zhang, H., Lin, W., Wang, Y., Xu, W., and Jia, S.: First simultaneous measurements of peroxyacetyl nitrate (PAN) and
557 ozone at Nam Co in the central Tibetan Plateau: impacts from the PBL evolution and transport processes, *Atmos. Chem.
558 Phys.*, 18, 5199-5217, 10.5194/acp-18-5199-2018, 2018.
- 559 Xu, Z., Xue, L., Wang, T., Xia, T., Gao, Y., Louie, P. K. K., and Luk, C. W. Y.: Measurements of Peroxyacetyl Nitrate at a
560 Background Site in the Pearl River Delta Region: Production Efficiency and Regional Transport, *Aerosol Air Qual. Res.*, 15,
561 833-841, 10.4209/aaqr.2014.11.0275, 2015.
- 562 Xue, L., Wang, T., Wang, X., Blake, D. R., Gao, J., Nie, W., Gao, R., Gao, X., Xu, Z., Ding, A., Huang, Y., Lee, S., Chen, Y.,
563 Wang, S., Chai, F., Zhang, Q., and Wang, W.: On the use of an explicit chemical mechanism to dissect peroxy acetyl nitrate
564 formation, *Environ. Pollut.*, 195, 39-47, 10.1016/j.envpol.2014.08.005, 2014.
- 565 Xue, L. K., Wang, T., Guo, H., Blake, D. R., Tang, J., and Zhang, X. C.: Sources and photochemistry of volatile organic
566 compounds in the remote atmosphere of western China: results from the Mt. Waliguan Observatory, *Atmos. Chem. Phys.*, 13,
567 8551-8567, 10.5194/acp-13-8551-2013, 2013.
- 568 Yang, X., Wu, K., Wang, H., Liu, Y., Gu, S., Lu, Y., Zhang, X., Hu, Y., Ou, Y., Wang, S., and Wang, Z.: Summertime ozone
569 pollution in Sichuan Basin, China: Meteorological conditions, sources and process analysis, *Atmos. Environ.*, 226,
570 10.1016/j.atmosenv.2020.117392, 2020.
- 571 Ye, C., Zhang, N., Gao, H., and Zhou, X.: Photolysis of Particulate Nitrate as a Source of HONO and NO_x, *Environ. Sci. Technol.*,
572 51, 6849-6856, 10.1021/acs.est.7b00387, 2017.
- 573 Yuan, J., Ling, Z., Wang, Z., Lu, X., Fan, S., He, Z., Guo, H., Wang, X., and Wang, N.: PAN–Precursor Relationship and Process
574 Analysis of PAN Variations in the Pearl River Delta Region, *Atmos.*, 9, 10.3390/atmos9100372, 2018.
- 575 Yukihiro, M., Hiramatsu, T., Bouteau, F., Kadono, T., and Kawano, T.: Peroxyacetyl nitrate-induced oxidative and calcium
576 signaling events leading to cell death in ozone-sensitive tobacco cell-line, *Plant Signal Behav.*, 7, 113-120,
577 10.4161/psb.7.1.18376, 2012.
- 578 Zeng, L., Fan, G. J., Lyu, X., Guo, H., Wang, J. L., and Yao, D.: Atmospheric fate of peroxyacetyl nitrate in suburban Hong Kong
579 and its impact on local ozone pollution, *Environ. Pollut.*, 252, 1910-1919, 10.1016/j.envpol.2019.06.004, 2019.
- 580 Zhai, S., Jacob, D. J., Franco, B., Clarisse, L., Coheur, P., Shah, V., Bates, K. H., Lin, H., Dang, R., Sulprizio, M. P., Huey, L. G.,
581 Moore, F. L., Jaffe, D. A., and Liao, H.: Transpacific Transport of Asian Peroxyacetyl Nitrate (PAN) Observed from Satellite:
582 Implications for Ozone, *Environ. Sci. Tech.*, 58, 9760-9769, 10.1021/acs.est.4c01980, 2024.



583 Zhang, G., Mu, Y., Zhou, L., Zhang, C., Zhang, Y., Liu, J., Fang, S., and Yao, B.: Summertime distributions of peroxyacetyl nitrate
584 (PAN) and peroxypropionyl nitrate (PPN) in Beijing: Understanding the sources and major sink of PAN, *Atmos. Environ.*,
585 103, 289–296, 10.1016/j.atmosenv.2014.12.035, 2015.

586 Zhang, J., Guo, Y., Qu, Y., Chen, Y., Yu, R., Xue, C., Yang, R., Zhang, Q., Liu, X., Mu, Y., Wang, J., Ye, C., Zhao, H., Sun, Q.,
587 Wang, Z., and An, J.: Effect of potential HONO sources on peroxyacetyl nitrate (PAN) formation in eastern China in winter, *J.*
588 *Environ. Sci. (China)*, 94, 81-87, 10.1016/j.jes.2020.03.039, 2020.

589 Zhang, J. M., Wang, T., Ding, A. J., Zhou, X. H., Xue, L. K., Poon, C. N., Wu, W. S., Gao, J., Zuo, H. C., Chen, J. M., Zhang, X.
590 C., and Fan, S. J.: Continuous measurement of peroxyacetyl nitrate (PAN) in suburban and remote areas of western China,
591 *Atmos. Environ.*, 43, 228-237, 10.1016/j.atmosenv.2008.09.070, 2009.

592 Zhu, J., Wang, S., Wang, H., Jing, S., Lou, S., Saiz-Lopez, A., and Zhou, B.: Observationally constrained modeling of atmospheric
593 oxidation capacity and photochemical reactivity in Shanghai, China, *Atmos. Chem. Phys.*, 20, 1217-1232, 10.5194/acp-20-
594 1217-2020, 2020.

595

596